

1 Millikelvin-precision temperature sensing for advanced  
2 cryogenic detectors

3 M. Antonova<sup>a</sup>, J. Capó<sup>a</sup>, A. Cervera<sup>a</sup>, P. Fernández<sup>a,2</sup>, M. Á. García-Peris<sup>a,1,\*</sup>, X.  
4 Pons<sup>b</sup>

<sup>a</sup>*Instituto de Fisica Corpuscular Catedratico Jose Beltran 2 E-46980 Paterna (Valencia) Spain*

<sup>b</sup>*CERN Espl. des Particules 1 1211 Meyrin Switzerland*

---

5 **Abstract**

Precise temperature monitoring —to the level of a few milli-Kelvin— is crucial for the operation of large-scale cryostats requiring a recirculation system. In particular, the performance of Liquid Argon Time Projection Chambers —such as those planned for the DUNE experiment— heavily relies on proper argon purification and mixing, which can be characterized by a sufficiently dense grid of high-precision temperature probes. In this article, a novel technique for the cross-calibration of Resistance Temperature Detectors (RTDs) in cryogenic liquids (argon and nitrogen) is presented, obtaining an unprecedented precision of 2.5 mK.

6 *Keywords:* Detectors, Liquid Argon, Cryogenics, Temperature, RTD, Purity,  
7 Computational Fluid Dynamics

---

8 **1. Introduction**

9 Precise temperature sensing is essential in large cryogenic detectors, where the circulation  
10 and purification of cryogenic liquids significantly impact overall detector performance.  
11 Uncontrolled temperature gradients in such systems can disrupt the cryostat dynamics  
12 and ultimately affect the experiment's physics sensitivity. In this work, we present the  
13 calibration procedure of a novel temperature monitoring system developed for a prototype  
14 of the future DUNE experiment.

---

\*Corresponding author

Email address: [miguel.garcia-peris@manchester.ac.uk](mailto:miguel.garcia-peris@manchester.ac.uk) (M. Á. García-Peris)

<sup>1</sup>now in the University of Manchester

<sup>2</sup>now at Donostia International Physics Center, DIPC

DUNE, which stands for Deep Underground Neutrino Experiment [2], is expected to begin taking data toward the end of the decade. It aims to perform comprehensive neutrino oscillation analyses —broadly exploring the Charge-Parity (CP) violation parameters phase-space and resolving the neutrino-mass hierarchy problem [6]. Its extensive physics program also includes searches for hypothetical proton decay channels [3], multi-messenger astronomy from supernovae and neutrino bursts [8], and explorations of Beyond the Standard Model (BSM) physics [7]. Utilizing the most powerful neutrino beam ever constructed, generated at Fermilab, the experiment adopts a long-baseline neutrino oscillation approach with two detectors. The Near Detector, also at Fermilab, will characterize the unoscillated neutrino beam. The Far Detector (FD), located in the Sandford Underground Research Facility (SURF), 1300 km away from the ND and 1.5 km underground, will measure the oscillated flux.

In the Phase I, DUNE Far Detector will consist of two Liquid Argon Time Projection Chambers (LArTPCs) and is anticipated to begin operations by 2029. DUNE phase II will complement with two more modules by mid 30's, aiming at a total fiducial mass of 40 kilotonnes. The detector technology has been established, with excellent tracking and calorimetric capabilities, in several smaller-scale experiments [10, 13]. The first demonstration of the technology at the kilotonne scale has been carried out at the CERN Neutrino Platform as part of the ProtoDUNE program. In particular, the ProtoDUNE Single-Phase (SP) experiment [1] replicated the components of the DUNE FD Horizontal Drift (HD) [4] configuration at a scale 1:1, using a total argon mass 20 times smaller (770 tonnes). It was operated from mid-2018 to mid-2020, constituting the largest monolithic LArTPC to ever constructed and operated up to date [5, 9].

During ProtoDUNE-SP operation, the level of impurities was kept way below 100 ppt oxygen equivalent using a cryogenic recirculation and purification system [1, 9]. This is critical in an LArTPC, as the 3D images generated by charged particles traversing the detector can be significantly degraded by impurities in the medium—such as nitrogen, oxygen, and water—which absorb ionization electrons, thereby deteriorating spatial resolution and introducing biases in energy measurements. Three purity monitors, based on the ICARUS design [25], were installed outside the active volume of the TPC to measure the electron lifetime, which is inversely related to the residual concentration of

46 impurities. They ran twice a day to monitor the argon purity and thus to provide the  
47 necessary corrections for posterior data analysis.

48 Achieving the necessary argon purity has been possible thanks to the studies based  
49 on computational fluid dynamic (CFD) simulations, and the experience gained with  
50 previous LArTPC demonstrators such as LAPD [11] and the 35-tonne prototype [12, 18],  
51 which have paved the way to operate large-scale cryostats requiring low concentrations  
52 of impurities. These studies have also shown that it exists a strong correlation between  
53 temperature and purity in the liquid argon volume. The distribution of impurities is  
54 insensitive to small ( $\mathcal{O} \sim 1$  K) absolute temperature variations, but strongly depends on  
55 the relative vertical temperature gradient. Since the bulk volume in the cryostats must  
56 be continuously mixed with the incoming purified argon to ensure uniform purification  
57 of the entire LAr volume, the temperature distribution serves as a clear indicator of  
58 the mixing process: a homogeneous temperature distribution suggests proper mixing,  
59 while large temperature gradients signal inadequate mixing. If the LAr bulk volume is  
60 not mixed appropriately, a stratification regime can develop: a significant portion of the  
61 liquid remains unpurified, generating ‘dead’ regions inside the detector. Thus, continuous  
62 monitoring of this temperature gradient can identify and mitigate potential failures of  
63 the purification system. In ProtoDUNE-SP, this gradient was predicted to be about 15  
64 mK by the CFD simulations [1, 4].

65 Even with homogeneous mixing, the CFD simulations predict that the concentration  
66 of impurities may vary across the cryostat volume, requiring a position-dependent correc-  
67 tion to the electron lifetime. The Purity Monitors themselves are intrusive objects which  
68 cannot be deployed inside the active volume, but rather only at a few well-defined loca-  
69 tions near the cryostat walls; thus, precise inference of the electron lifetime map requires  
70 alternative methods, as the one proposed in this article. A net of temperature sensors  
71 cross-calibrated to the <5 mK level should allow the measurement of a 15 mK tempera-  
72 ture gradient, which can be used to constrain CFD simulations, providing a data-driven  
73 prediction of the impurity concentration. The main limitations of this new approach are  
74 the precision of the cross-calibration of the temperature sensors and the accuracy of the  
75 simulations. In this article, precise temperature monitoring for ProtoDUNE-SP will be  
76 described, with particular emphasis on sensor calibration in the laboratory.

77    **2. The temperature monitoring system of ProtoDUNE-SP**

78    ProtoDUNE-SP [1] was the Single-Phase demonstrator of DUNE Far Detector HD mod-  
79    ule [4]. The elements constituting the TPC, its associated readout electronics and the  
80    photon detection system, were housed in a 8x8x8 m<sup>3</sup> cryostat that contained the LAr that  
81    served both as target and detector material. The cryostat, a free-standing steel-framed  
82    vessel with an insulated double membrane, is based on the technology used for liquefied  
83    natural gas storage and transport. A cryogenic system maintains the LAr at a stable  
84    temperature of about 87 K by operating at a slight and constant over-pressure. It also  
85    ensures the required purity level by means of a closed-loop process that recovers the evap-  
86    orated argon, recondenses it, filters it, and recirculates it back into the cryostat, keeping  
87    the LAr level at about 7.3 m from the bottom membrane. ProtoDUNE-SP was exposed  
88    to a charged particle test-beam from October to November 2018, and later recorded cos-  
89    mic rays until January 2020 [5, 9]. It was finally emptied and decommissioned during  
90    Summer 2020.

91       In order to understand the LAr behaviour inside the cryostat and validate the CFD  
92    simulations, 92 high-precision temperature sensors were installed inside ProtoDUNE-  
93    SP, near the active volume. These sensors were distributed in two vertical arrays, or  
94    Temperature Gradient Monitors (TGM), and two horizontal grids below and above the  
95    TPC, respectively. Three elements were common to all systems: sensors, cables and  
96    readout electronics. RTD technology [22] was chosen for this application. It consists of a  
97    metallic element whose resistance changes with temperature. This resistance is measured  
98    by feeding the RTD with a known current and measuring the resulting voltage. Based on  
99    previous experience from other prototypes [12], Lake Shore PT102 platinum sensors [21]  
100   with 100 Ω resistance at room temperature were chosen. Sensors were mounted on a  
101   52x14 mm<sup>2</sup> PCB with an IDC-4 connector, such that they could be plugged-in at any  
102   time. Several versions of the PCB have been explored, finally converging to the one  
103   shown in Fig. 1, which minimizes the contact of the sensor with the PCB while keeping  
104   the sensor protected.

105      A careful choice of the readout cable and the connections are essential to obtain the  
106   required temperature precision. See for example Ref. [22] for a detailed description. A  
107   custom cable made by Axon [14] was used. It consists of four American Wire Gauge

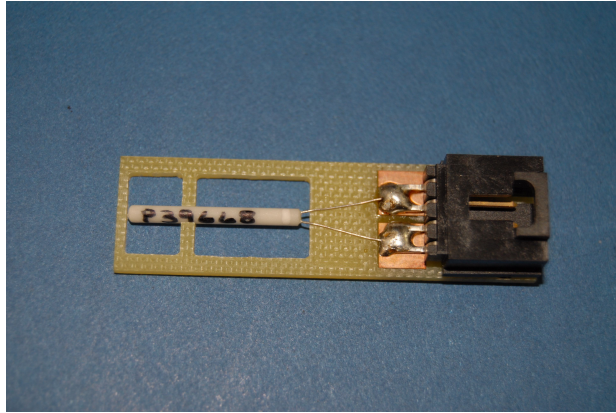


Figure 1: PCB support with temperature sensor and IDC-4 connector. The transition from two wires at the sensor to 4 wires at the readout is clearly seen. The sensor has a length of 2 cm.

108 (AWG) 28 teflon-jacketed copper wires, forming two twisted pairs, with a metallic ex-  
 109 ternal shield and an outer teflon jacket. The outer diameter of the cable is 3.7 mm.  
 110 Teflon was chosen for its good thermal properties and low out-gassing. The metallic  
 111 external shield (connected to the readout in one end and left floating at the sensor's end)  
 112 and the twisted pairs are crucial to reduce the effect of external electromagnetic noise  
 113 pick-up. When RTDs are far from the voltmeter, the resistance of cables and connectors  
 114 are added to the one of the sensor, biasing the temperature measurement. This bias  
 115 can be subtracted to some level, but cannot be fully controlled since the resistance of  
 116 those elements also depends on temperature. To minimise the impact of this effect a four  
 117 wire-terminal readout is employed [22], such that the voltage is measured in the vicinity  
 118 of the RTD.

119 The last common element is the readout system, consisting of a very precise 1 mA  
 120 current source to excite the sensors and a 24 bits ADC to measure the voltage. The  
 121 readout system will be described in detail in Section 3.

122 As previously mentioned, ProtoDUNE-SP CFD simulations predict vertical tempera-  
 123 ture gradients as low as 15 mK [1]. A relative precision better than 5 mK was required to  
 124 validate and tune those simulations with sufficient confidence. Three main ingredients are  
 125 necessary to obtain such a precision: i) cryogenically rated, high-accuracy temperature  
 126 probes suitable for LAr applications., ii) a very precise readout system, and iii) accurate

127 and stable long-term calibration, both for the readout and the sensors. As mentioned  
128 above, two TGMs were deployed in ProtoDUNE-SP: one could be moved vertically and  
129 hence calibrated *in situ*, while the other one—static—fully relied on a prior calibration  
130 in the laboratory. In this article, the calibration of the static TGM [17] sensors is de-  
131 scribed in detail. This device consists of a vertical array of 48 sensors, installed 20 cm  
132 away from the lateral field cage.

133 The calibration was performed once in spring 2018 (a few months before the operation  
134 of ProtoDUNE-SP), and several times after ProtoDUNE-SP decommissioning. In this  
135 article the calibration setup, procedure and results will be described in detail. Compar-  
136 ison between the different calibration campaigns will be addressed, revealing important  
137 information about systematic uncertainties and RTD ageing.

### 138 3. Readout system

139 A precise and stable electronic readout system is needed to achieve the required precision.  
140 In previous versions of the calibration system, each sensor was connected to a different  
141 and independent electronic circuit and thus, fed by a different current and read by a  
142 different ADC channel. It was soon realized that the measured temperature difference  
143 between any two pairs of sensors was heavily affected by the electronic offset between  
144 channels. This offset was not constant, and showed dependence on ambient temperature  
145 and humidity, which affected both the current source and the ADC, generating variations  
146 of tens of mK for the measurement of a single calibration constant between two sensors.  
147 A modified version of an existing PT100 mass temperature readout system, developed  
148 at CERN for one of the LHC experiments [16], was adapted to address this issue. The  
149 system consists of an electronic circuit that includes:

- 150 • A precise and accurate 1 mA current source for the excitation of the temperature  
151 sensors based on an application of the Texas Instruments precise voltage reference  
152 REF102CU with a possibility to adjust  $\pm 10\text{nA}$  with Keithley 2001 multimeter [15,  
153 23].
- 154 • A multiplexing circuit based on the Analog Devices ADG1407BRUZ multiplexer  
155 with ultralow internal resistance in an 8-channel differential configuration. By in-  
156 tegrating three multiplexers, the readout circuit supports simultaneous acquisition

157 from 24 channels. The multiplexing circuit and the current source are assembled  
158 on a single card (see Fig. 2).

- 159
- 160 • A readout system based on National Instruments Compact RIO-FPGA device [19]  
161 equipped with a NI-9238 analogue input module that provide 24 bits resolution over  
162 1 volt range [20]. By programming the Van Dusen equation the readout calculates  
163 the temperature in Kelvin units. The Compact RIO also drives the control bits of  
the multiplexers

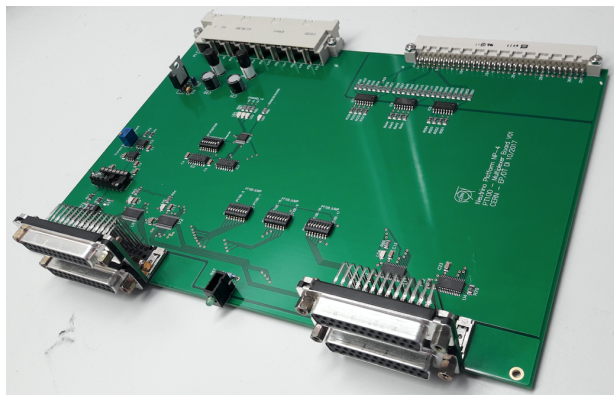


Figure 2: Current source and multiplexing card with 24 channels.

164 One of the features of the readout circuit is the serialization of the current source ex-  
165 citation for all the sensors connected to the same board, such that the same current is  
166 delivered to all of them. Multiplexing the signal of the sensors such that they can be  
167 readout by the same ADC channel minimises the residual offset due to the electronics.  
168 This system was used during the calibration campaigns presented in this article and also  
169 for the temperature measurements during ProtoDUNE-SP operation.

170 The readout was not considered a potential source of bias during the calibration  
171 campaign prior to the installation in ProtoDUNE-SP (see Sec. 4) and it was not studied  
172 in detail at that time. However, in order to improve the calibration results following  
173 ProtoDUNE-SP operation, a more detailed study of the readout system was conducted  
174 prior to the calibration campaigns presented in 5. In particular, the twelve channels  
175 (7-18) used for sensor calibration were investigated. It was found that, despite the use of  
176 the multiplexing system, a small residual offset between channels persists. Fig. 3 shows

177 the offsets of channels 8-18 with respect to channel 7, computed using twelve 20-ohm  
 178 precision resistors with a low Temperature Coefficient of Resistance (TCR)<sup>3</sup> precision  
 179 resistors, with an equivalent temperature of 76 K. Two of those, High Precision 1 (HP1)  
 180 and High Precision 2 (HP2), are selected as the measurement samples and connected  
 181 to the reference channel (7) and the channel being calibrated (from 8-18), while leaving  
 182 all other channels connected to other secondary resistors to let the current flow through  
 183 the system. The readout offset between channel 7 and channel X,  $\Delta T_{7-X}^{readout}$ , is then  
 184 computed using the results of two consecutive measurements:

- 185 1. HP1 in channel 7 and HP2 in the channel X being calibrated. The offset between  
 186 the measured temperatures is

$$\Delta T_{7-X}^A = T_X^{HP2} - T_7^{HP1} + \Delta T_{7-X}^{readout}. \quad (1)$$

- 187 2. HP2 channel 7 and HP1 in the channel X being calibrated. The offset between the  
 188 measured temperatures is

$$\Delta T_{X-7}^B = T_X^{HP1} - T_7^{HP2} + \Delta T_{7-X}^{readout}. \quad (2)$$

189 Because of the very low TCR of the resistors, it can be assumed that the resistances  
 190 are constants in these two measurements ( $T_7^{HP1} = T_X^{HP1}$  and  $T_7^{HP2} = T_X^{HP2}$ ). Thus,  
 191 the offset between channels 7 and X can be computed as the average between those two  
 192 measurements:

$$\Delta T_{7-X}^{readout} = \frac{\Delta T_{7-X}^A + \Delta T_{X-7}^B}{2}. \quad (3)$$

193 The results in Fig. 3, show an offset of up to 2.5 mK when comparing directly with  
 194 channel 7, while the offset between any other two channels is below 1 mK, indicating  
 195 a special feature of this channel. Error bars in that figure correspond to the standard  
 196 deviation of four independent measurements (repeatability) of the same offset (see Fig. 3).  
 197 As it can be observed the error is below 0.5 mK, what probes the great repeatability of

---

<sup>3</sup>The temperature coefficient of resistance is defined as the change in resistance per unit resistance per degree rise in temperature. Typically  $\pm 5\text{ppm}/^\circ\text{C}$ .

198 the readout. These offsets are more likely due to parasitic resistances in the different  
 199 lines that are multiplexed. This finding allowed a correction to the measurements taken  
 200 during the subsequent calibration campaigns, improving the obtained precision.

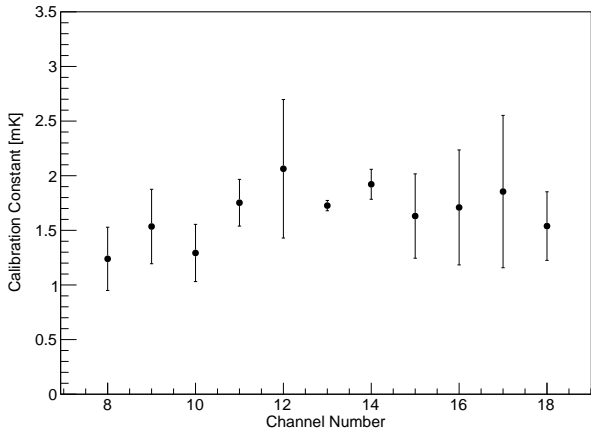


Figure 3: Offset between readout channels 8-18 and channel 7, used as reference. Points correspond to the mean of the 4 independent measurements and the error bars are their standard deviation.

#### 201 4. Calibration before the installation in ProtoDUNE-SP

202 The Lake Shore Cryotronics company provides PT102 RTDs with a temperature ac-  
 203 curacy of about 0.1 K, which is insufficient for ProtoDUNE-SP's requirements. While  
 204 the company offers additional calibration to the 10 mK level, the cost is prohibitive.  
 205 R&D on sensor calibration was identified as a crucial ingredient for the success of the  
 206 ProtoDUNE-SP temperature monitoring system. For this particular application, sensor  
 207 calibration consists in finding the temperature offset between any pair of sensors when  
 208 exposing them to the same temperature. The experimental setup used for the calibra-  
 209 tion of RTDs before their installation in ProtoDUNE-SP had two main components: i)  
 210 the readout system used to monitor the sensor's temperature (described in the previous  
 211 section) and ii) the cryogenics vessel and the associated mechanical elements used to  
 212 put sensors together under stable and homogeneous cryogenics conditions. They were  
 213 developed to achieve a relative calibration with a precision better than 5 mK.

214 *4.1. Experimental setup*

215 The mechanics of the calibration setup evolved significantly from the initial tests to the  
216 final Static TGM calibration campaign. This evolution was primarily driven by the need  
217 to improve offset stability and repeatability. The final configuration (see Fig. 4) consisted  
218 of the following components:

- 219 • A polystyrene vessel formed by an outer box with dimensions  $35 \times 35 \times 30 \text{ cm}^3$  and  
220 4.5 cm thick walls, and a dedicated polystyrene cover, complemented by extruded  
221 polystyrene panels glued into the inner walls and floor of the outer box, to conform  
222 an inner empty volume of  $10 \times 10 \times 20 \text{ cm}^3$ .
- 223 • A  $10 \times 10 \times 20 \text{ cm}^3$  3D printed polyactic acid (PLA) box with two independent con-  
224 centric volumes, placed in the inner volume of the polystyrene vessel. Its purpose  
225 is twofold: i) to contain LAr, since polystyrene is porous to it, and ii) to create an  
226 smaller inner volume with further insulation and less convection.
- 227 • A cylindrical aluminum capsule, to be placed in the inner volume of the PLA box,  
228 with 5 cm diameter, 12 cm height and 1 mm thin walls. It had a circular aluminum  
229 cover with a small opening to extract the cables and to allow LAr to penetrate  
230 inside. The capsule was used to slowly bring sensors to cryogenic temperatures by  
231 partial immersion in LAr with no liquid inside, minimizing thermal stress. Alu-  
232 minium was chosen for its high thermal conductivity.
- 233 • A 3D printed PLA support for four sensors, to be placed inside the aluminum  
234 capsule, keeping sensors always in the same position with respect to each other and  
235 to the capsule walls.

236 The system described above ensures sufficiently stable and homogeneous conditions  
237 within the inner volume, with three levels of insulation: the outer polystyrene vessel and  
238 two PLA box LAr volumes. The aluminium capsule is key to this system and its usage  
239 constituted a turning point in the R&D since it minimises thermal shocks, which were  
240 identified as the main limiting factor for the repeatability of the sensor's offsets. Indeed,  
241 variations of several tenths of mK were observed during initial tests without the capsule.  
242 The problem was attributed to thermal shocks when, after many immersions in LN<sub>2</sub>, one

<sup>243</sup> of the sensors suffered a dramatic change in its offset (see Fig. 5). Examination at the  
<sup>244</sup> microscope revealed cracks in the outer RTD ceramics (see Fig. 6).



Figure 4: Final calibration setup. Left: polystyrene box with PLA box and aluminum capsule. Middle: aluminum capsule. Right: Sensor's support with four sensors.

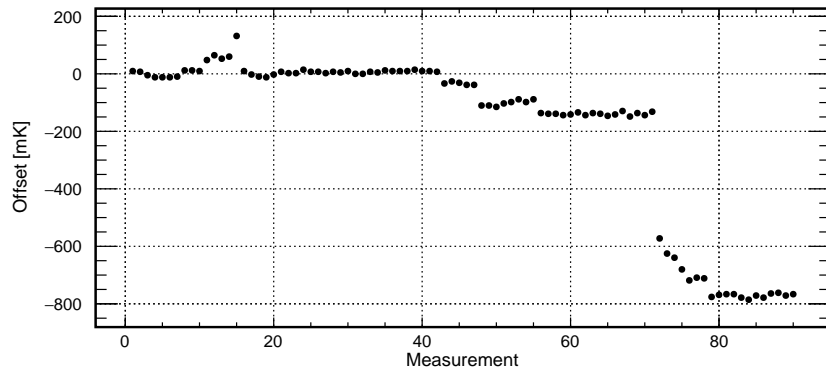


Figure 5: Offset between two sensors for 90 immersions in LN<sub>2</sub>. A temperature drop of approximately 800 mK is observed around the 70th immersion point.

<sup>245</sup> *4.2. Calibration procedure*

<sup>246</sup> The calibration procedure relies on the assumption that all sensors in the capsule are at  
<sup>247</sup> the same temperature. This limits the number of RTDs in a single run to four, since  
<sup>248</sup> i) they should be as close as possible to each other and ii) as far as possible from the  
<sup>249</sup> capsule walls (the sensor closer to the wall could be biased). Two different methods,  
<sup>250</sup> described schematically in Fig. 7, were used to cross-calibrate all 48 sensors in runs of 4  
<sup>251</sup> sensors:

<sup>252</sup> **1. Reference method:** all sensors are calibrated with respect to a reference one, in  
<sup>253</sup> sets of three sensors (the fourth one would be the reference sensor, which must be  
<sup>254</sup> present in all runs). In total there are sixteen calibration sets.

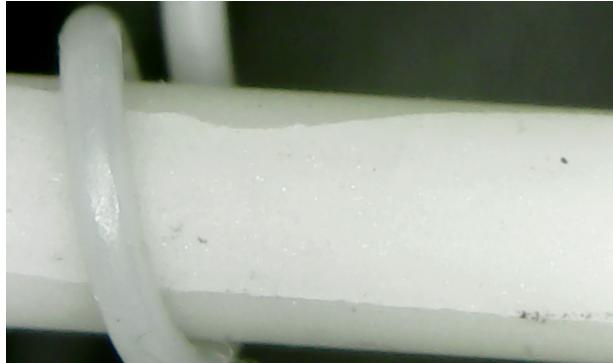


Figure 6: Cracks observed with the microscope in the ceramic of the sensor.

255     **2. Tree method:** Four different sets of sensors can be cross-calibrated by performing  
 256     a second round of measurements with a single promoted sensor from each of those  
 257     four sets. Since there are 16 sets in total, a third round of measurement is needed  
 258     to cross-calibrate the four sets in the second round.

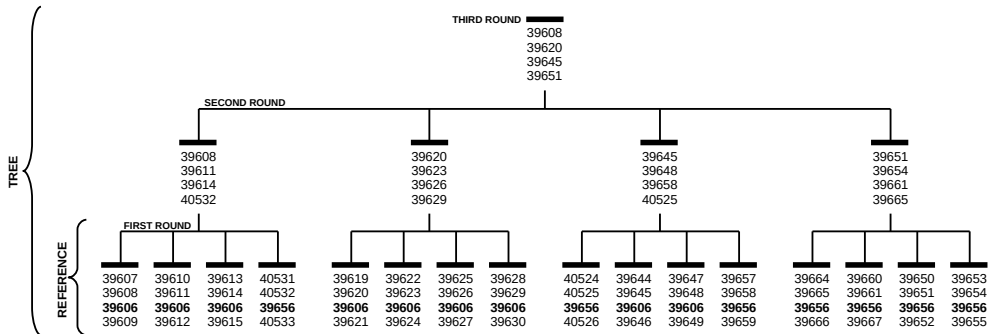


Figure 7: Schematic view of calibration sequence. Each number represents a different RTD, and the numbers in bold represent the reference sensors. The first round consists on a direct calibration respect to a reference sensor. The second and third rounds are needed to relate all sensors independently of the reference sensor.

259     The reference method was expected to be more precise since any two sensors were  
 260     related through a single intermediate sensor (the reference one), while for the tree method  
 261     the relation between any two sensors required more than one intermediate sensor. For  
 262     example, the offset between sensors  $i$  and  $j$  in different sets, related through sensors  $k$   
 263     and  $l$  in the second round, would be  $\Delta T_{ij} = \Delta T_{ik} + \Delta T_{kl} + \Delta T_{lj}$ . For sensors related  
 264     through the third round an additional term should be added, further increasing the offset

265 uncertainty.

266 Offset repeatability is a critical parameter to understand, as the laboratory calibration  
267 must remain valid when applied to the actual detector. To study this, four independent  
268 calibration runs were performed for each set of four sensors. However, due to concerns  
269 about thermal fatigue in the primary reference sensor—subjected to 64 thermal cycles  
270 over the four repeatability runs—three secondary reference sensors were employed to  
271 regularly monitor its response and ensure reliability over time.

272 The following procedure is applied for each set of four sensors. First, they are placed  
273 inside the aluminium capsule. The central connector closer to the red one is used for  
274 the reference sensor. These positions are easily called by numbers from 1 (orange) to 4  
275 (red), as shown in Fig. 8-left.

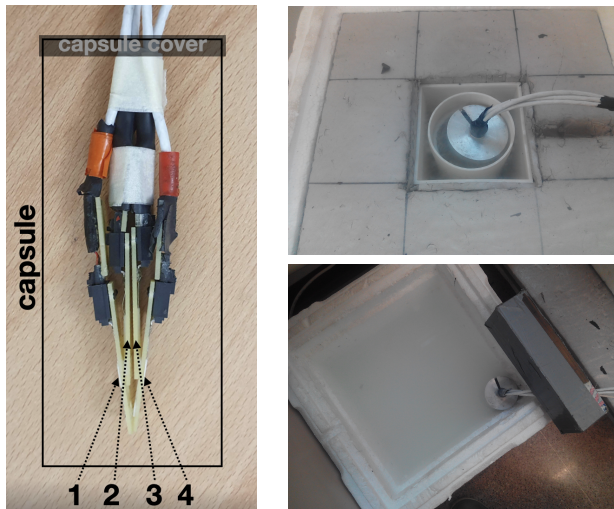


Figure 8: Left: Picture of sensor order inside the flask. Position 1 corresponds to highest serial number and 4 to lowest; position 3 is reserved to reference sensor. Top: Flask partially introduced in LAr. Bottom: Flask partially introduced in room water to warm up sensors before performing a new measurement.

276 After filling the PLA box with liquid argon, the aluminum capsule is partially im-  
277 mersed (see Fig. 8-right-top), allowing the air inside to cool down gradually. This setup  
278 prevents the sensors from coming into direct contact with liquid argon, instead inducing  
279 a slow cooldown through the surrounding cold gas atmosphere, thereby avoiding thermal  
280 shock. When the monitored temperature approaches the one of LAr (< 95 K), which  
281 takes about 15 minutes, the capsule is completely immersed, being filled with liquid.

282 The PLA box is then completely filled with LAr to account for evaporation during the  
283 cool-down phase. Finally, the polystyrene vessel is closed using the polystyrene lid. The  
284 calibration run actually begins at that point and lasts for 40 minutes.

285 When the measurement is finished, the capsule is extracted from the liquid, emptied  
286 of LAr and partially immersed into another polystyrene box filled with water at room  
287 temperature (see Fig. 8-right-bottom). The warm-up process takes about ten minutes.  
288 When sensors have reached a temperature around 250 K a new independent calibration  
289 run can start.

290 Fig. 9 shows the typical evolution of the temperature for the four sensors in the  
291 capsule during the warm-up and cool-down processes. A sudden fall to 87 K is observed  
292 at minute 32, which corresponds to total immersion of the sensors in LAr. Notice also  
293 that two of the sensors have lower temperature during the cool-down process; those are  
294 sensors 1 and 4, the ones closer to the capsule walls.

295 For each set of sensors the procedure described above is repeated four times, resulting  
296 in four independent measurements of the same offset. These measurements are used to  
297 compute a mean offset value and its standard deviation (repeatability from now on).

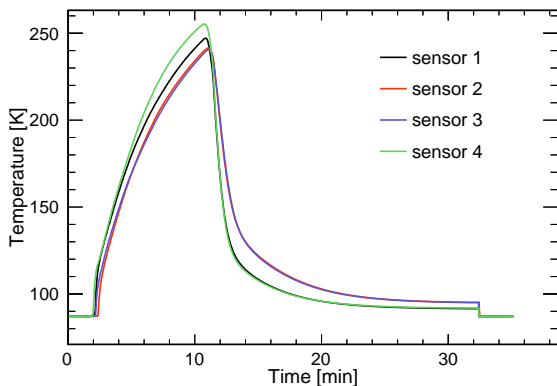


Figure 9: Temperature evolution between two calibration runs, showing the warm-up and cool-down phases of the four temperature sensors inside the capsule. Sensors 1 and 4 are located closest to the capsule walls.

298 *4.3. Calibration results*

299 Here we present the results of the calibration using both calibration methods, a study of  
300 the consistency of these results, and a preliminary estimation of the systematic uncer-

301 tainty of the calibration process.

#### 302 4.3.1. Results on the first round of measurements

303 Fig. 10 shows the offset of three different sensors with respect to the reference sensor as  
304 a function of time, and for four independent calibration runs. The offset is more stable  
305 for the sensor closer to the reference (position 2), while external sensors (positions 1  
306 and 4) present larger variations, but show similar patterns between them. This effect  
307 is attributed to the geometry of the system, with sensors at different heights and not  
308 symmetrically positioned with respect to the capsule walls. This was taken into account  
309 when developing the second version of the system, presented in Sec. 5.

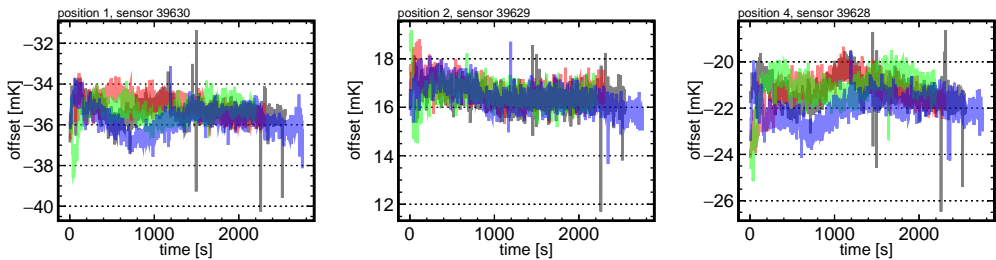


Figure 10: Offset between the reference sensor and each of the three sensors in a set, as a function of time. Each colour represents an independent calibration run.

310 The mean offset for each sensor and each calibration run is calculated as the average  
311 over the time interval between 1000 and 2000 seconds, identified as the most stable region  
312 for the majority of the runs. The standard deviation of the four means is taken as the  
313 uncertainty, hereafter referred to as repeatability. As shown in Fig. 11, the uncertainties  
314 are generally below 1 mK, demonstrating the high level of repeatability achieved in the  
315 calibration process.

#### 316 4.3.2. Time walk correction for reference sensors

317 Time evolution of the response of sensor 39606 was studied by periodically (every  $\sim$ 20  
318 immersions) computing its offset with respect to three secondary reference sensors, 39603,  
319 39604 and 39605. For each of those additional calibrations, two runs were taken instead  
320 of four in order to minimize thermal fatigue of the reference sensor. As shown in Fig. 12-  
321 left, the offset, computed as the mean of those two runs, varies linearly at a rate of  
322 0.07 mK/immersion, which suddenly increases to 0.22 mK/immersion after 60 runs.

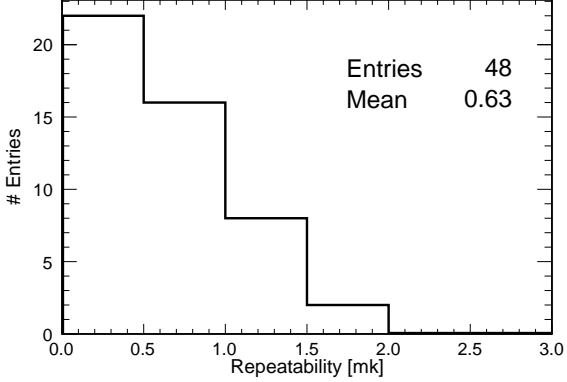


Figure 11: Distribution of the repeatability for calibration runs in the first round.

This change in the slope may be related with to the frequency of immersions, which increased from 3/day to 5/day. Sensor 39606 was initially used for other purposes, and the calibration of the 48 sensors conforming the static TGM started approximately at immersion 40. Given this change in its response, sensor 39606 was substituted by 39656 as primary reference for the last quarter of the TGM calibration in order to avoid further fatigue and potential untraceable behaviour. The evolution of the new reference sensor is shown in Fig. 12-right. It is worth noting that the same slopes are valid for the three secondary reference sensors in both cases, supporting the idea that the change observed in the offsets can be exclusively attributed to thermal fatigue of the reference sensor.

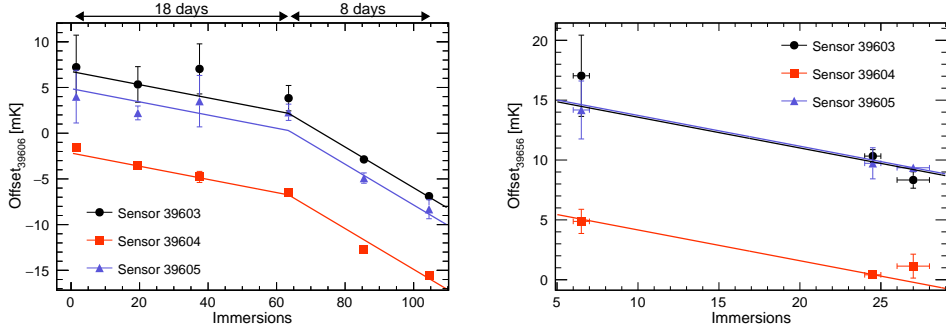


Figure 12: Offset between the reference sensors (39606 on the left panel and 39656 on the right panel) and the three secondary references as a function of the number of immersions. Offsets for sensor 39604 have smaller errors because of its position inside the capsule. Solid lines correspond to the parametrization in Eq. 4.

332        The zero intercept in both panels of Fig. 12 corresponds to the unbiased offset (or the  
 333        offset at  $N_{\text{immersions}} = 0$ ) of each of the secondary reference sensors with respect to the  
 334        primary reference. In order to compute the unbiased offset for a sensor  $s$ , a time walk  
 335        correction after  $N$  immersions is parameterised as:

$$\Delta T_{s,06}(N=0) = \begin{cases} \Delta T_{s,06}(N) + (0.072 \pm 0.003) * N & N < 63.5 \\ \Delta T_{s,06}(N) + (0.072 \pm 0.003) * 63.5 + \\ +(0.223 \pm 0.007) * (N - 63.5) & N > 63.5, \end{cases} \quad (4)$$

$$\Delta T_{s,56}(N=0) = \Delta T_{s,56}(N) + (0.168 \pm 0.007) * N. \quad (5)$$

336        All sensors can be related to the same primary reference sensor, 39606, adding the  
 337        unbiased offset between sensors 39606 and 39656,  $\Delta T_{56,06}(N=0)$ , to sensors calibrated  
 338        with respect to 39656. By averaging over the three secondary reference sensors, the value  
 339        obtained is  $\Delta T_{56,06}(N=0) = -9.19 \pm 0.13$  mK.

#### 340        4.3.3. Results on the reference method

341        Fig. 13 shows the offset of all sensors with respect to the 39606 reference. As it can  
 342        be noticed, the dispersion of the offsets is compatible with 0.1 K, the value quoted by  
 343        the vendor. Fig. 14-left shows the distribution of the repeatability of the computed  
 344        calibration constants after applying the different corrections, showing an average value  
 345        below 1 mK.

#### 346        4.3.4. Results on the tree method

347        The offsets are computed in this case with respect to an arbitrary reference among all  
 348        sensors being calibrated. Selecting as reference a sensor present in the third round (see  
 349        Fig. 7) minimizes the number of operations required to compute the offsets, thereby  
 350        reducing the associated uncertainty. Sensor 39645 was chosen as reference. Fig. 14-right  
 351        shows the distribution of the repeatability of the computed calibration constants, the  
 352        mean of which is slightly below the one obtained for the reference method. Thus, it  
 353        is confirmed that despite the higher number of intermediate sensors to relate any two  
 354        sensors, the additional uncertainty introduced by the time walk correction makes the tree  
 355        method superior to the reference method. Moreover, the reference method introduces a  
 356        —not yet known— systematic error associated to the time wall correction model.

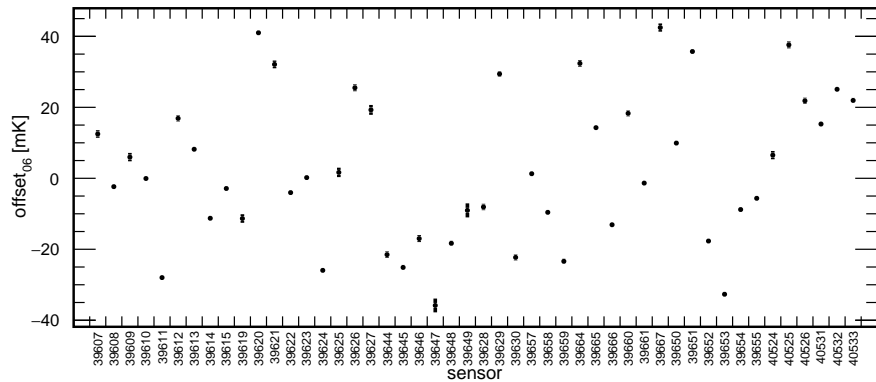


Figure 13: Offset of each sensor with respect to reference sensor 39606 using the reference method.

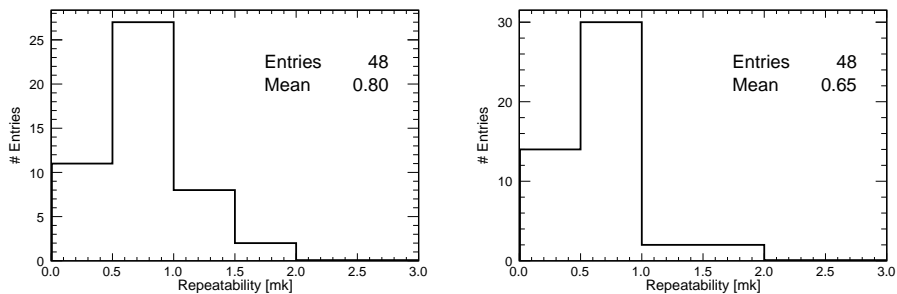


Figure 14: Left: repeatability distribution for the reference method. Right: repeatability distribution for tree method.

357    4.3.5. *Consistency cross-check and error estimation*

358    The uncertainties presented are, on average, smaller than 1 mK and correspond to the  
359    standard deviation of the four independent measurements of each calibration constant,  
360    combined with the error propagation from the required corrections: time-walk correction  
361    for the reference method, addition of calibration constants for the tree method, and the  
362    uncorrected electronic residual offset common to calibration methods. These corrections  
363    likely include unknown systematic effects impacting the final calibration constants, which  
364    need to be added to the systematic uncertainty associated to the assumption of homoge-  
365    neous temperature inside the capsule. To estimate the overall precision of the calibration,  
366    the following cross-check was performed. The calibration strategy yields two independent  
367    values for each sensor's calibration constant—one obtained from the reference method  
368    and the other from the tree method. For the sixteen sensors used in the second round of  
369    the calibration tree, these two values are linearly independent because they are derived  
370    from different sets: the reference method relies solely on first-round runs, while the tree  
371    method uses only second and third-round runs for those sensors. Therefore, these sixteen  
372    sensors provide an effective basis for estimating the calibration procedure's precision by  
373    comparing the results obtained from the two methods.

374    By construction, the result of subtracting the calibration constants obtained in the  
375    two methods should be compatible with the offset between sensors 39645 and 39606,  
376     $\Delta T_{45,06} = \Delta T_{s,06} - \Delta T_{s,45} = T_{45} - T_{06}$ , used as reference for the tree and reference  
377    methods respectively. This offset is found to be  $-25.1 \pm 0.7$  mK by direct measurement  
378    of the two sensors (see 10th column in Fig. 7 and 13). Fig. 15 shows this benchmark with  
379    (left) and without (right) time walk corrections for the 16 sensors aforementioned, probing  
380    the self-consistency of this correction. The standard deviation of this distribution, 2.4  
381    mK, is an estimation of the quadratic sum of the total uncertainty of both calibrations.  
382    Assuming that the reference sensor method has a larger uncertainty than the tree method  
383    due to the time walk correction, an upper limit of 1.7 mK for the total error of the tree  
384    method can be assumed. In the same way, this is the inferior limit for the total error of  
385    the reference method. In both cases, these errors are less than half of what was originally  
386    required for the temperature monitoring system in DUNE FD-HD.

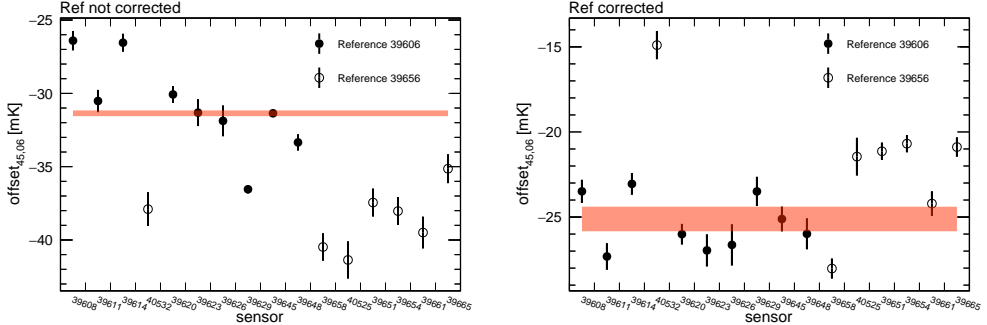


Figure 15:  $\Delta T_{45,06}$  computed through all sensors of the second round of the calibration procedure. Left: not applying corrections. Right: applying corrections. A clear improvement is obtained using the corrections on the reference sensor. The red line represents the expected value of this calibration constant.

### 387 5. Re-calibration after ProtoDUNE-SP operation

388 After ProtoDUNE-SP decommissioning in 2020, temperature sensors were disconnected  
 389 from the TGM and re-calibrated several times (see Table 1), using both LAr and LN2  
 390 as cryogenic liquid. **Two sensors were damaged during PD-SP decommissioning. Those**  
 391 **were not replaced until the LAr-2023 calibration campaign.** The comparative analysis of  
 392 those re-calibrations not only offers insights into the long-term stability of the sensors but  
 393 also elucidates any potential dependencies on the choice of the cryogenic liquid. Although  
 394 DUNE will use LAr, massive RTD calibration would benefit from using LN2, given its  
 395 higher accessibility and lower cost.

Date	Cryogenic liquid	# Sensors in capsule
March 2018	LAr	4
February 2022	LN2	14
March 2023	LN2	14
July 2023	LAr	14

Table 1: Calibration runs with indication of the date, the cryogenic liquid used and the number of sensors inside the capsule.

396 In this section, a description of the setup used for these new calibrations, the changes  
 397 applied to the procedure as well as the results and conclusions of these calibrations are  
 398 presented.

399    *5.1. Evolution of the calibration setup*

400    The FD-HD module will be equipped with over 500 precision sensors [4], making the use  
401    of the current calibration setup impractical, as it can accommodate only four sensors  
402    simultaneously. Significant modifications have been introduced in order to increase this  
403    number to twelve, while maintaining the precision achieved during the 2018 calibration  
404    campaign. This was accomplished by positioning sensors at the same height, to avoid  
405    any potential vertical gradient, and following a cylindrical configuration, under the as-  
406    sumption that convection inside the capsule has rotational symmetry. This symmetry  
407    is also kept outside the capsule in all concentric cryogenic containers, having added a  
408    fourth independent volume which should further reduce convection inside the inner cap-  
409    sule. This notable advancement greatly streamlines the calibration process and serves  
410    to reduce both statistical and systematic errors associated with the procedure. Fig. 16  
411    shows the different elements of the new calibration setup, which are described below:

- 412    • A polystyrene box with dimensions  $55 \times 35 \times 30 \text{ cm}^3$  and 4.5 cm thick walls with  
413    a dedicated cover of the same material.
- 414    • Extruded polystyrene rectangles with a cylindrical hole of 12.5 cm diameter and  
415    25 cm height, to conform the inner volume.
- 416    • A PTFE container with 12.5 cm diameter, 25 cm height and 2 mm thick walls to  
417    fit in the hole left in the box. The approximate volume is 2 L.
- 418    • A 3D printed PLA cylinder with two independent concentric volumes, placed inside  
419    the PTFE container.
- 420    • A cylindrical aluminum capsule to be placed in the inner volume of the PLA cylin-  
421    der. It has 7 cm diameter, 14 cm height and 1 mm thick walls.
- 422    • A 3D printed PLA holder for 14 sensors, 12 of them forming a circle (the ‘corona’)  
423    and the other 2 at the center, to be used as references. This support can be attached  
424    to the aluminum capsule at a fixed height. Cables are naturally extracted from the  
425    top of the assembly. A detailed view of this holder can be found in Fig. 16.
- 426    • The readout electronics, described in Sec. 3 has been retained from the previous  
427    setup.

- 428     • A more cost effective cable with similar performance has been used. Produced by  
 429     TempSens [24], it has four twisted cables instead of two separated twisted pairs  
 430     and an additional Kapton insulation layer between the shielding mesh and the four  
 431     conductors. Its diameter is 2.7 mm.

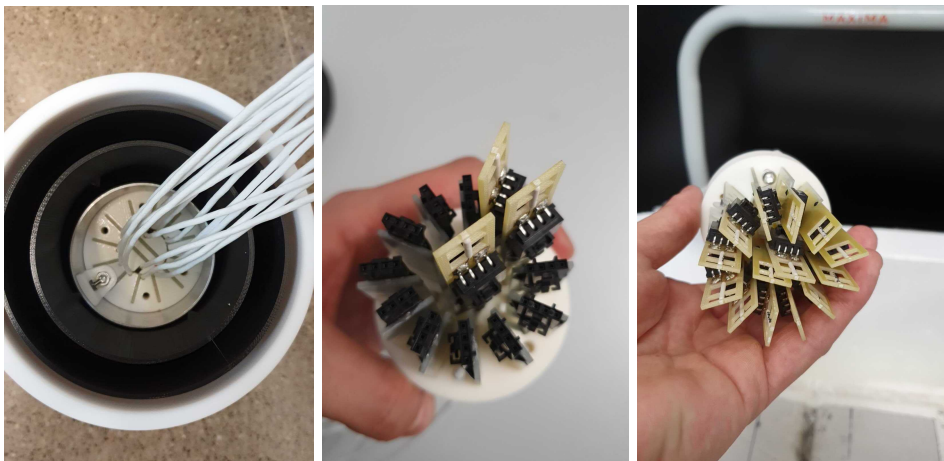


Figure 16: Left: The four concentric volumes of the calibration setup. Center: A view of one of the references and two corona sensors. Right: The 12 corona sensors plus the 2 references.

432     *5.2. Calibration procedure*

433     The sensor support was originally designed to accommodate two reference sensors in  
 434     the center (see Fig. 16), enabling both the reference and tree calibration methods.  
 435     However, it was soon observed that temperature variations between corona and reference  
 436     sensors were significantly larger than those between any two corona sensors. This effect  
 437     is attributed to the convection pattern inside the capsule, which is expected to have  
 438     rotational invariance, and hence favour sensors disposed following a cylindrical symmetry.  
 439     This can be observed in Fig. 17-left, where the offset between two corona sensors is  
 440     nearly constant in time in four independent measurements, and in Fig. 17-right, where  
 441     the offset between a corona and a reference sensor shows a more chaotic behaviour.  
 442     Consequently, only the ‘tree’ calibration method was considered during the calibrations  
 443     after ProtoDUNE-SP decommissioning.

444     The new calibration tree, shown in Fig. 18, contemplates four 12-sensors sets in the  
 445     first round, and a unique second round with three promoted sensors from each of the

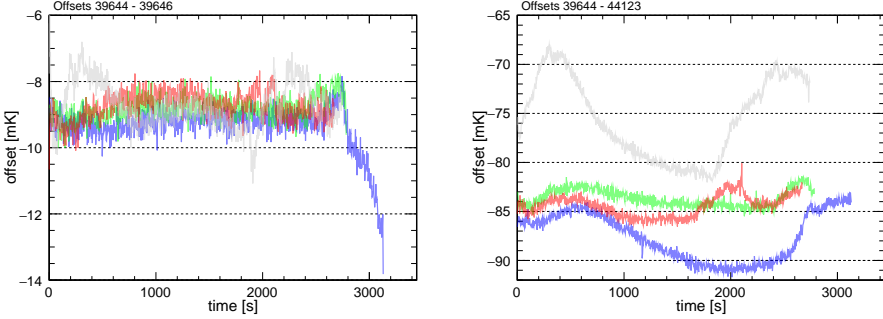


Figure 17: Left: The 4 measured offsets between two arbitrary sensors in the corona. Right: The 4 measured offsets between a sensor in the corona and one of the references, at the center.

446 sets in the first round. With this scheme, promoted sensors only suffer 8 baths, avoiding  
 447 the necessity of a time-walk correction.

448 The experimental procedure is similar to the one presented in Sec. 4. Two small  
 449 variations were introduced. First, the several concentric containers are cooled down  
 450 for 40 minutes before introducing the aluminium capsule for the first time in a day,  
 451 slightly improving the results of the first calibration run. Second, the warm up process  
 452 is accelerated using a heat gun, avoiding the use of water.

### 453 5.3. Calibration results

454 A sensor from the second round is chosen as the reference, as this minimizes the number of  
 455 operations required for the non-promoted sensors. Since each set includes three promoted  
 456 sensors, there are three **linearly independent** ways to compute the offset relative to the  
 457 reference for the nine non-promoted sensors in that set. The calibration constant for these  
 458 sensors is calculated as the weighted average of the three “paths”, with its uncertainty  
 459 given by the standard deviation of these three values. The offset uncertainty used in the  
 460 weighted average for each of the three paths is computed by quadratically summing the  
 461 individual uncertainties (as in Fig. 19) of all terms contributing to the offset along that  
 462 specific path. Sensor 40525 is adopted as the reference for the remainder of the analysis.

463 Fig. 19 shows the distribution of the repeatability (defined in Sec. 4.3.1) for the three  
 464 new calibrations mentioned in Table 1. **AÑADIR AQUÍ EL PORQUÉ LAR2023 TIENE**  
 465 **47 entries.** In all three cases the uncertainty is slightly above 1 mK. Mean values are  
 466 larger than the ones obtained in the 2018 calibration campaign. This is attributed to

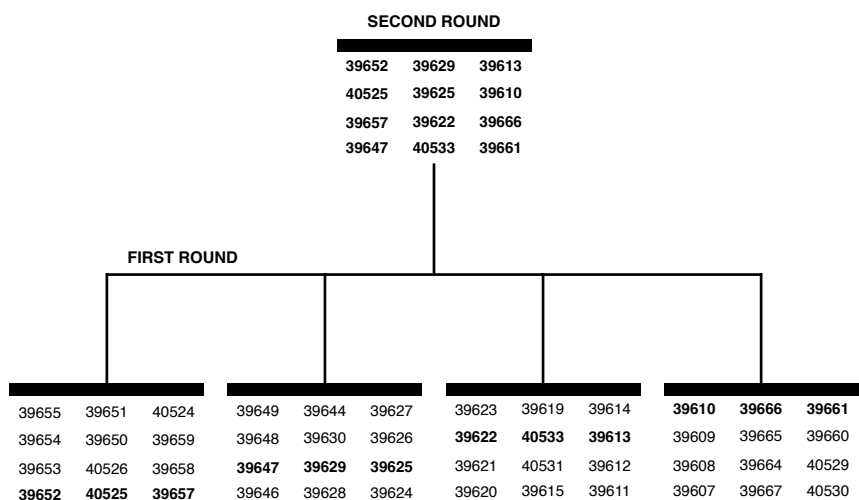


Figure 18: Schematic of the calibration sequence used with the new setup. Each of the sets contains 12 sensors, all of them placed in the corona, plus 2 references at the center. Sensors in bold in the first round are promoted to the second round.

467 the increased capsule size and the larger distance between sensors inside the capsule.  
 468 This hypothesis is supported by Fig. 20, showing the repeatability as a function of the  
 469 distance to the reference sensor in the corona for a particular measurement. However,  
 470 there is no substantial difference between the repeatability obtained for LN2 and LAr  
 471 calibrations.

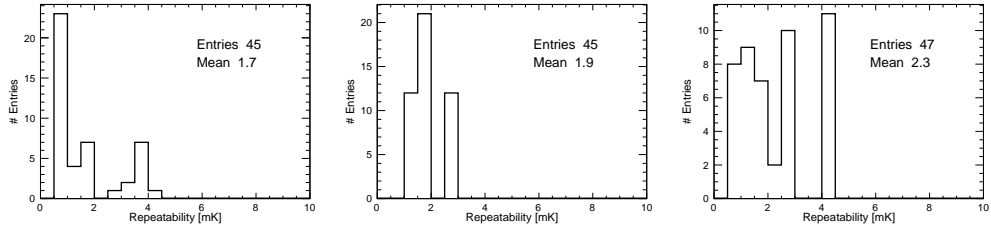


Figure 19: Repeatability distribution for the new calibrations. Left: LN2-2022. Middle: LN2-2023, Right:LAr-2023

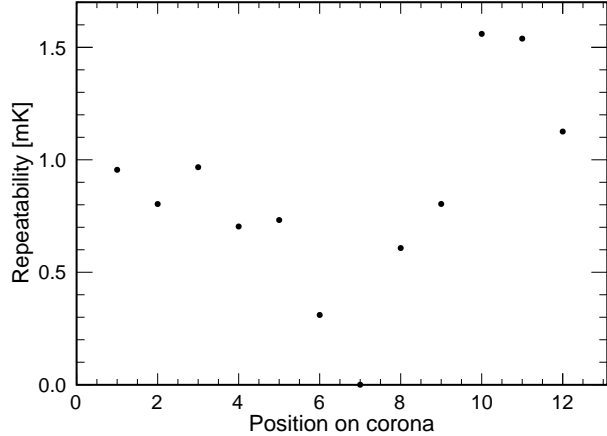


Figure 20: Repeatability as a function of position in the corona for the first set of the LAr-2023 calibration campaign. Sensor in position 7 is taken as reference.

472 Comparison between LN2 and LAr calibrations can also be used to understand the  
 473 dependence of the calibration constants on the absolute temperature. This is shown  
 474 in Fig. 21 along with other comparisons between calibration campaigns. The standard  
 475 deviation of the distribution is lower when comparing two calibrations in the same liquid  
 476 (LN2 in this case). However no bias is observed when comparing calibrations in two

477 different liquids, indicating that offsets are insensitive to a 10 K variation in absolute  
 478 temperature.

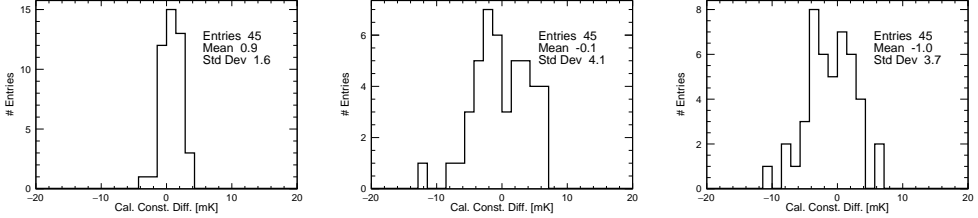


Figure 21: Difference between offsets for two calibrations. Left: LN2-2022 and LN2-2023. Middle: LN2-2022 and LAr-2023. Right: LN2-2023 and LAr-2023.

479 Ageing and long term stability have also been addressed. The left panel of Fig. 21  
 480 shows no difference between the offsets calculated in LN2 with a delay of one year. A bet-  
 481 ter understanding of this effect is achieved by comparing with the LAr-2018 calibration,  
 482 as shown in the next section.

#### 483 5.4. Comparison between new and old calibrations

484 Fig. 22 shows the distribution of the offset difference between the LAr-2018 and LAr-  
 485 2023 calibrations. The mean of the distribution is  $-0.1 \pm 0.6$  mK, excluding any relevant  
 486 systematic drift. The standard deviation of the distribution, 4.3 mK, is only slightly  
 487 larger than the ones obtained in the comparison between newer calibrations, which could  
 488 be due to the unknown contribution of the uncorrected readout offsets, pointing to small  
 489 or non-existing ageing effects. This can also be observed in Table 2, summarizing the  
 490 results of all possible comparisons between calibration campaigns, showing the mean and  
 491 standard deviation of those comparisons. The lowest standard deviation, 1.6 mK, is  
 492 obtained for the LN2-2022 to LN2-2023 combination, which is somehow expected since  
 493 i) the cryogenic liquid is the same, ii) ageing should be small since there is only one year  
 494 difference and iii) having use the same readout channels, readout offsets cancel out.  
 495 The difference between the constants obtained in two calibration campaigns can be used  
 496 to estimate the total calibration error. Since ProtoDUNE Horizontal Drift (ProtoDUNE-  
 497 HD), the next iteration of the ProtoDUNE-SP detector, and DUNE will use LAr, the  
 498 best estimation of the error would come from a LAr to LAr comparison close in time to  
 499 the actual detector running. Being this combination not available, three other combina-

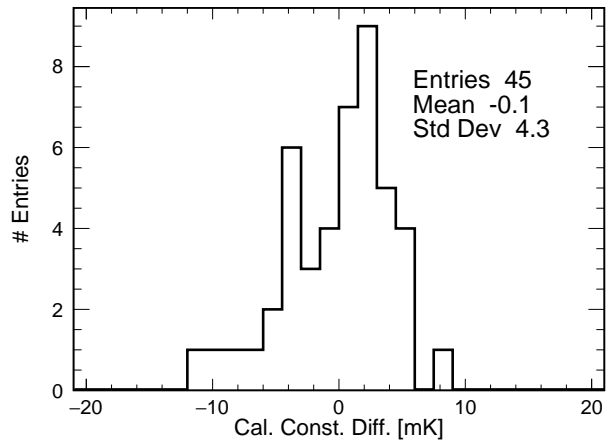


Figure 22: Difference between offsets for LAr-2018 and LAr-2023 calibration campaigns.

	LAr-2018	LN2-2022	LN2-2023	LAr-2023
LAr-2018	-	0.0, 3.5	0.9, 3.9	-0.1, 4.3
LN2-2022	-	-	0.9, 1.6	-0.1, 4.1
LN2-2023	-	-	-	-1.0, 3.7
LAr-2023	-	-	-	-

Table 2: Mean and standard deviation of the difference between the calibration constants obtained in two calibration campaigns.

500 tions can be used. The comparison between the LN2 calibrations from 2022 and 2023  
501 yields a standard deviation of 1.6 mK, which should represent the quadratic sum of the  
502 individual calibration errors. Assuming equal errors for both campaigns, this implies a  
503 single calibration error of approximately 1.13 mK. In this case, readout channel offsets  
504 cancel out, although real fluctuations in those offsets still contribute to the estimated  
505 single calibration error. The comparison between LAr calibrations from 2018 and 2023  
506 provides further insight, with a standard deviation of 4.3 mK, corresponding to a sin-  
507 gle calibration error of about 3.0 mK. However, this value includes uncorrected readout  
508 offsets as well as potential effects from sensor ageing. Finally, comparing the new LAr  
509 and LN2 calibration campaigns avoids issues related to readout offsets and ageing but  
510 may be affected by the differences in cryogenic liquids. These comparisons yield a similar  
511 standard deviation around 3.8 mK, implying a single calibration error of approximately  
512 2.7 mK. This value thus establishes an upper limit on the LAr calibration error. In  
513 summary, the individual calibration error in LAr is estimated to lie between 1.6 and  
514 3.0 mK. This range is consistent with an independent estimate of 1.7 mK obtained using  
515 a different method for the LAr-2018 calibration (see Sec. 4.3.5).

## 516 6. Conclusions

517 The DUNE experiment will require the construction and operation of the largest cryostats  
518 ever used in a particle physics experiment. This makes the continuous measurement of  
519 temperature gradients in liquid argon crucial for monitoring the stability of the cryogenics  
520 system and for detector calibration. R&D on the calibration of RTD probes started in  
521 2017, leading to promising results for sensors installed in the DUNE prototype at CERN.

522 The first setup proved the viability of the method, obtaining a calibration error of 1.7  
523 mK. A key component was the readout electronics, with an intrinsic resolution better  
524 than 0.5 mK in the comparison between two channels. The mechanics was also crucial,  
525 with several insulation layers consisting of independent concentric volumes, ensuring  
526 minimal convection in the inner volume. Sensors were contained in an aluminium capsule,  
527 enabling slow cool-down and warm-up processes, found to be fundamental to guarantee  
528 the integrity of the sensors and to minimize the effect of ageing.

529 The calibration system was later enhanced to accommodate the large-scale calibration

530 required for the DUNE detectors. The capacity of the inner capsule was increased from  
531 4 to 14 sensors, while improvements were made to the insulation and symmetry of the  
532 system to minimize temperature differences between sensors. The new system has slightly  
533 worst repeatability for sensors in the same set, but reduces the statistical and systematic  
534 errors associated to the calibration tree, needed to relate any two sensors in different  
535 calibration sets. Calibration with the new setup has achieved a precision in the range of  
536 1.6-3.0 mK, substantially better than the 5 mK DUNE requirement.

537 Another difference between the new and old calibrations is the use of a different  
538 cryogenic liquid. While DUNE will use LAr, LN2 is cheaper, simplifying the process of  
539 massive calibration for DUNE detectors. The 10 K difference between those liquids has  
540 a minimal effect on the calibration constants.

541 A comparison of the four calibration campaigns has provided valuable insights into  
542 aging effects, with no evidence of RTD aging observed over a five-year period. This  
543 highlights the stability and reliability of the PT-102-based system.

## 544 7. Acknowledgments

545 The present research has been supported and partially funded by Conselleria d’Innovació,  
546 Universitats, Ciència i Societat Digital, by the Fundación ‘La Caixa’, and by MICINN.  
547 The authors would also like to thank all the people involved in the installation,  
548 commissioning and operation of ProtoDUNE-SP, specially to Stephen Ponders.

## 549 References

- 550 [1] Abi, B., et al. (DUNE), 2017. The Single-Phase ProtoDUNE Technical Design Report  
551 [arXiv:1706.07081](https://arxiv.org/abs/1706.07081).
- 552 [2] Abi, B., et al. (DUNE), 2020a. Deep Underground Neutrino Experiment (DUNE), Far Detector  
553 Technical Design Report, Volume I Introduction to DUNE. JINST 15, T08008. doi:10.1088/  
554 1748-0221/15/08/T08008, [arXiv:2002.02967](https://arxiv.org/abs/2002.02967).
- 555 [3] Abi, B., et al. (DUNE), 2020b. Deep Underground Neutrino Experiment (DUNE), Far Detector  
556 Technical Design Report, Volume II: DUNE Physics [arXiv:2002.03005](https://arxiv.org/abs/2002.03005).
- 557 [4] Abi, B., et al. (DUNE), 2020c. Deep Underground Neutrino Experiment (DUNE), Far Detector  
558 Technical Design Report, Volume IV: Far Detector Single-phase Technology. JINST 15, T08010.  
559 doi:10.1088/1748-0221/15/08/T08010, [arXiv:2002.03010](https://arxiv.org/abs/2002.03010).
- 560 [5] Abi, B., et al. (DUNE), 2020d. First results on ProtoDUNE-SP liquid argon time projection  
561 chamber performance from a beam test at the CERN Neutrino Platform. JINST 15, P12004.  
562 doi:10.1088/1748-0221/15/12/P12004, [arXiv:2007.06722](https://arxiv.org/abs/2007.06722).
- 563 [6] Abi, B., et al. (DUNE), 2020e. Long-baseline neutrino oscillation physics potential of the DUNE  
564 experiment. Eur. Phys. J. C 80, 978. doi:10.1140/epjc/s10052-020-08456-z, [arXiv:2006.16043](https://arxiv.org/abs/2006.16043).
- 565 [7] Abi, B., et al. (DUNE), 2021a. Prospects for beyond the Standard Model physics searches  
566 at the Deep Underground Neutrino Experiment. Eur. Phys. J. C 81, 322. doi:10.1140/epjc/  
567 s10052-021-09007-w, [arXiv:2008.12769](https://arxiv.org/abs/2008.12769).

- 568 [8] Abi, B., et al. (DUNE), 2021b. Supernova neutrino burst detection with the Deep Under-  
 569 ground Neutrino Experiment. *Eur. Phys. J. C* 81, 423. doi:10.1140/epjc/s10052-021-09166-w,  
 570 [arXiv:2008.06647](https://arxiv.org/abs/2008.06647).
- 571 [9] Abud, A.A., et al. (DUNE), 2022. Design, construction and operation of the ProtoDUNE-SP Liquid  
 572 Argon TPC. *JINST* 17, P01005. doi:10.1088/1748-0221/17/01/P01005, [arXiv:2108.01902](https://arxiv.org/abs/2108.01902).
- 573 [10] Acciarri, R., et al. (MicroBooNE), 2017. Design and Construction of the MicroBooNE Detector.  
 574 *JINST* 12, P02017. doi:10.1088/1748-0221/12/02/P02017, [arXiv:1612.05824](https://arxiv.org/abs/1612.05824).
- 575 [11] Adamowski, M., et al., 2014. The Liquid Argon Purity Demonstrator. *JINST* 9, P07005. doi:10.  
 576 1088/1748-0221/9/07/P07005, [arXiv:1403.7236](https://arxiv.org/abs/1403.7236).
- 577 [12] Adams, D.L., et al., 2020. Design and performance of a 35-ton liquid argon time projection chamber  
 578 as a prototype for future very large detectors. *JINST* 15, P03035. doi:10.1088/1748-0221/15/03/  
 579 P03035, [arXiv:1912.08739](https://arxiv.org/abs/1912.08739).
- 580 [13] Amerio, S., et al. (ICARUS), 2004. Design, construction and tests of the ICARUS T600 detector.  
 581 *Nucl. Instrum. Meth. A* 527, 329–410. doi:10.1016/j.nima.2004.02.044.
- 582 [14] Axon, . Axon custom cables. URL: [https://www.axon-cable.com/en/00\\_home/00\\_start/00\\_index.aspx](https://www.axon-cable.com/en/00_home/00_start/00_index.aspx). last visited: 2022-10-01.
- 583 [15] application bulletin, B.B., . Implementation and applications of current sources and current re-  
 584 ceivers. URL: <https://www.ti.com/lit/an/sboa046/sboa046.pdf?ts=1712062207089>. last visited:  
 585 2024-04-02.
- 586 [16] Chojnacki, E., 2009. A Multiplexed RTD Temperature Map System for Multi-Cell SRF Cavities,  
 587 in: SRF2009, p. 232.
- 588 [17] García-Peris, M.A., 2018. ProtoDUNE T-Gradient development and calibration. Master's thesis.  
 589 Valencia U. doi:10.2172/1780813.
- 590 [18] Hahn, A., Adamowski, M., Montanari, D., Norris, B., Reichenbacher, J., Rucinski, R., Stewart,  
 591 J., Tope, T. (LBNE), 2016. The LBNE 35 Ton Prototype Cryostat, in: 2014 IEEE Nuclear Sci-  
 592 ence Symposium and Medical Imaging Conference and 21st Symposium on Room-Temperature  
 593 Semiconductor X-ray and Gamma-ray Detectors. doi:10.1109/NSSMIC.2014.7431158.
- 594 [19] Instruments, N., a. Compactrio systems. URL: <https://www.ni.com/es/shop/compactrio.html>.  
 595 last visited: 2024-04-02.
- 596 [20] Instruments, N., b. Ni-9238. URL: <https://www.ni.com/es-es/shop/model/ni-9238.html>. last  
 597 visited: 2024-04-02.
- 598 [21] LakeShore, . Platinum sensors applications. URL: <https://www.lakeshore.com/products/categories/overview/temperature-products/cryogenic-temperature-sensors/platinum>. last  
 599 visited: 2023-05-18.
- 600 [22] Minco, . Resistance thermometry. URL: <https://www.minco.com/wp-content/uploads/Resistance-Thermometry.pdf>. last visited: 2023-05-18.
- 601 [23] Tektronix, . Keithley 2001 digit high performance multimeter. URL: [https://download.tek.com/datasheet/1KW-73954-1\\_2001-2002\\_DMM\\_Datasheet\\_080323.pdf](https://download.tek.com/datasheet/1KW-73954-1_2001-2002_DMM_Datasheet_080323.pdf). last visited: 2024-04-02.
- 602 [24] TempSens, . Rtd cables. URL: <https://tempsens.com/catalog/cables-wires/rtd-triad-cables.html>. last visited: 2024-03-15.
- 603 [25] Xiao, Y. (DUNE), 2021. Purity monitoring for ProtoDUNE-SP. *J. Phys. Conf. Ser.* 2156, 012211.  
 604 doi:10.1088/1742-6596/2156/1/012211.